Lab on a Chip

Dynamic Article Links

Cite this: *Lab Chip*, 2011, **11**, 4152

www.rsc.org/loc

PAPER

Automated and temperature-controlled micro-PIV measurements enabling long-term-stable microchannel acoustophoresis characterization

Per Augustsson,†[a] Rune Barnkob,†[b] Steven T. Wereley,[c] Henrik Bruus[b] and Thomas Laurell[ad]

Received 15th July 2011, Accepted 14th September 2011
DOI: 10.1039/c1lc20637k

We present a platform for micro particle image velocimetry (μPIV), capable of carrying out full-channel, temperature-controlled, long-term-stable, and automated μPIV-measurement of microchannel acoustophoresis with uncertainties below 5% and a spatial resolution in the order of 20 μm. A method to determine optimal μPIV-settings for obtaining high-quality results of the spatially inhomogeneous acoustophoretic velocity fields of large dynamical range is presented. In particular we study the dependence of the results on the μPIV interrogation window size and the number of repeated experiments. The μPIV-method was further verified by comparing it with our previously published particle tracking method. Using the μPIV platform we present a series of high-resolution measurements of the acoustophoretic velocity field as a function of the driving frequency, the driving voltage, and the resonator temperature. Finally, we establish a direct and consistent connection between the obtained acoustophoretic velocity fields, and continuous flow mode acoustophoresis, commonly used in applications.

I. Introduction

Microchannel acoustophoresis has received increasing interest within life sciences as an efficient, gentle and label-free method to manipulate cells and microbeads. Since the first microengineered continuous flow acoustophoretic particle filters,[1–4] many applications of microchannel acoustophoresis have emerged, including separation of erythrocytes from lipid particles,[5] bioaffinity purification using functionalized microbeads,[6] raw milk quality control,[7] cell cycle synchronization,[8] acoustic tweezers for cell patterning,[9] and cell sorting using surface acoustic waves.[10] In parallel, the fundamental physics of acoustophoretic microdevices, acoustofluidics, have been studied, such as particle trajectory analyses,[11,12] whole-chip imaging of acoustic resonances,[13] investigation of separation efficiencies,[14] surface acoustic wave generation of standing waves,[15] multi-mode resonance chips,[16] frequency modulated actuation,[17] on-chip integration with magnetic separators,[18] and measurement of acoustic properties of cells.[19]

A more complete understanding of the fundamental physics remains a core issue in the further development of acoustofluidics in general and acoustophoresis in particular. To achieve this, quantitative, high-resolution, stable, and reproducible measurements of acoustophoretic motion are needed. In a recent paper,[20] we developed a method based on single-particle tracking and curve-fitting to *in situ* determine the local acoustophoretic pressure amplitude and energy density for a specific one-dimensional, transverse acoustic resonance. However, due to a relatively high statistical uncertainty, the method is not appropriate for extending to a more general, two-dimensional, acoustic resonance field.

Hagsäter *et al.* showed that whole-chip micro-particle image velocimetry (μPIV) is a strong tool for analyzing two-dimensional microchannel acoustophoresis.[13] However, the time-consuming process associated with μPIV measurements of time-dependent inhomogeneous particle distributions and the lack of stable devices have hurdled any systematic measurement of the dependence on the system parameters.

In this work we present a μPIV setup capable of automated, quantitative, high resolution, and accurate full-chip measurements of microchannel acoustophoresis. The μPIV analysis is optimized and evaluated, and the method displays conformity with our earlier reported particle tracking algorithm. Moreover, the stability of the platform is investigated, and especially the temperature dependence of the acoustic field is characterized experimentally. The platform is then utilized for assessment of the acoustic field for different driving amplitudes and frequencies, and it is demonstrated that large segments of the acoustophoresis channel can be measured to capture the global features

[a]*Department of Measurement Technology and Industrial Electrical Engineering, Lund University, PO-Box 118, S-221 00 Lund, Sweden*
[b]*Department of Micro- and Nanotechnology, Technical University of Denmark, DTU Nanotech, Building 345 B, DK-2800 Kongens Lyngby, Denmark*
[c]*School of Mechanical Engineering, Purdue University, West Lafayette, IN, USA*
[d]*Department of Biomedical Engineering, Dongguk University, Seoul, South Korea*
† These authors contributed equally to this work.

of the acoustic resonances. Finally, continuous flow experiments are carried out to establish the strong link between local acoustic field-strength and the overall particle focusing efficiency of the device.

II. Background theory

A. Microchannel acoustophoresis

The background theory for microchannel acoustophoresis, based on the paper by Gorkov[21] and the textbooks by Lighthill,[22] Pierce,[23] and Bruus,[24] is presented in our previous work.[20] Briefly, we consider a silicon/glass chip containing a microchannel filled with an aqueous solution of particles. A piezo transducer is attached to the chip, such that when applying an ac voltage U_{pp} at a MHz frequency f, the piezo element vibrates and induces a time-harmonic ultrasound pressure field $p_1\exp(-i\omega t)$ and velocity field $\boldsymbol{v}_1\exp(-i\omega t)$, where we use the complex time-harmonic notation (implicitly assumed in the following), and where $\omega = 2\pi f$ is the angular frequency. As the viscosity of the carrier liquid has a negligible influence on the acoustic radiation forces on the large 5-μm-diameter tracer particles used in this work, the pressure and velocity field inside the microchannel are governed by simple linear acoustics of inviscid fluids, *i.e.* the Helmholtz wave equation for the pressure and potential flow for the velocity.

The acoustically soft water inside the channel surrounded by the acoustically hard silicon/glass chip forms an acoustic cavity. This implies that acoustic resonances occur for certain specific frequencies ω_j, $j = 1, 2, 3, \ldots$, where the average acoustic energy density inside the cavity is several orders of magnitude larger than at other frequencies $\omega \neq \omega_j$. By tuning the applied frequency to $\omega = \omega_j$, the acoustic forces become so strong that they in a reliable way can be used to manipulate particles suspended in the carrier liquid. The exact values of the resonance frequencies ω_j depend on the geometry of the acoustic cavity and of the material parameters of the liquid in the cavity as well as the surrounding material.

Products of the first-order acoustic fields give rise to two second-order effects, which persist even after time averaging: The acoustic radiation force acting on particles in suspension, and the acoustic streaming acting on the carrier liquid itself. The radiation force is the only second-order effect of importance in this work, *cf.* ref. 20, and this force is particularly strong at driving frequencies near the resonance frequencies.

Given the pressure field p_1 and velocity field $\boldsymbol{v}_1$ it is possible to calculate the acoustic radiation force on a spherical particle with volume $V = (4\pi/3)a^3$ and radius a much smaller than the acoustic wavelength λ. Both for biological cells and for microbeads used as tracers we are in this limit. The material parameters, with subscripts "wa" for the water and "p" for the particle, enter as the compressibility ratio $\tilde{\kappa} = \kappa_p/\kappa_{wa}$ in the compressibility factor f_1, and the density ratio $\tilde{\rho} = \rho_p/\rho_{wa}$ in the density factor f_2,

$$f_1 = 1 - \tilde{\kappa}, \quad f_2 = \frac{2\tilde{\rho}-2}{2\tilde{\rho}+1}. \tag{1}$$

The general expression for the time-averaged acoustic radiation force $\boldsymbol{F}_{ac}$ is a gradient of a potential,[21]

$$\boldsymbol{F}_{ac} = -V\boldsymbol{\nabla}\left[f_1\frac{\langle p_1^2\rangle}{2\rho_{wa}c_{wa}^2} - f_2\frac{3}{4}\rho_{wa}\langle v_1^2\rangle\right]. \tag{2}$$

For the special case of a standing transverse wave of wavenumber $k_y = 2\pi/\lambda$, the acoustic pressure amplitude is given by $p_a = 2\sqrt{E_{ac}\rho_{wa}c_{wa}^2}$, where E_{ac} is the acoustic energy density. Defining $\Phi = \frac{1}{3}f_1 + \frac{1}{2}f_2$, the corresponding pressure field p_1, the acoustophoretic force F_y, tracer-particle velocity u_y and transverse path $y(t)$ of the particle are given by[20]

$$p_1 = p_a\cos(k_y y), \tag{3a}$$

$$F_y = 4\pi\Phi a^3 k_y E_{ac}\sin(2k_y y), \tag{3b}$$

$$u_y = \frac{2\Phi}{3\eta}a^2 k_y E_{ac}\sin\left(2k_y y\right), \tag{3c}$$

$$y(t) = \frac{1}{k_y}\arctan\left\{\tan\left[k_y y(0)\right]\exp\left[\frac{4\Phi}{3\eta}\left(k_y a\right)^2 E_{ac}t\right]\right\}. \tag{3d}$$

To obtain a strong and stable acoustic resonance for a given piezo transducer, the following points must be taken into consideration. The electronic oscillator driving the transducer must have a stable frequency f and peak-to-peak voltage U_{pp}. The acousto-mechanical contact between the transducer and the chip must be stable and acoustically loss-free, preferably by using a hard epoxy glue. The amount of silicon/glass surrounding the microchannel should be minimized to maximize the ratio of acoustic energy inside the microchannel to the acoustic energy in the bulk. The use of soft materials connected to the chip (as *e.g.* fluidic tubing) must be kept to a minimum to reduce acoustic loses. The temperature of the chip must be kept constant as the temperature dependence of the mechanical properties of the chip (speed of sound, density, Young's modulus, and Poisson's ratio) translate into a temperature dependence of the resonance frequency, and hence of the acoustic energy in the microchannel.

B. μPIV measurements of acoustophoresis

μPIV is a flow measurement technique for obtaining detailed measurements of the velocities of groups of tracer particles

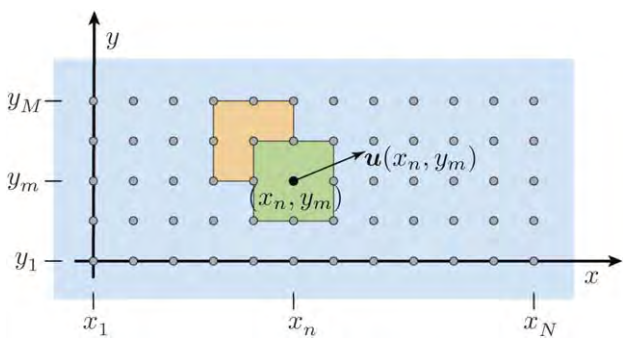

Fig. 1 Sketch of a given image frame (blue rectangle) containing $N \times M$ interrogation windows (green square) of size $S \times S$ pixel centered around the discrete grid points (x_n, y_m), gray circles. Neighboring interrogation windows overlap by 50% (light orange square). The μPIV interrogation window at each grid point results in a 2D velocity vector $u(x_n, y_m)$, black arrow.

(microbeads) in microfluidic systems.[25–29] It is based on digital image frames that, as sketched in Fig. 1, are sub-divided into interrogation windows centered around (x_n, y_m) and containing $S \times S$ pixel (rectangular area can be chosen) at positions $\boldsymbol{r}_{\mathrm{pix}}$ with intensity $I(x_n, y_m, t, \boldsymbol{r}_{\mathrm{pix}})$ at time t. The core of the μPIV technique is the discrete cross-correlation function C formed by the pixel intensities I from two interrogation windows (denoted an image pair), separated by a short time interval Δt,

$$C(x_n, y_m, t, \Delta t, \Delta \boldsymbol{r}) = \frac{1}{S^2} \sum_{\boldsymbol{r}_{\mathrm{pix}}}^{S^2} I\left(x_n, y_m, t, \boldsymbol{r}_{\mathrm{pix}} + \Delta \boldsymbol{r}\right) I\left(x_n, y_m, t + \Delta t, \boldsymbol{r}_{\mathrm{pix}}\right). \quad (4)$$

The pixel off-set $\Delta \boldsymbol{r}$ is varied until a maximum value of C is found, $\max_{\Delta \boldsymbol{r}}(C) = C(\Delta \boldsymbol{r}_{\max})$. This pixel displacement is then a measure of the local displacement of the tracer particles, and the corresponding particle velocity is given by $\boldsymbol{u}(x_n, y_m) = \Delta \boldsymbol{r}_{\max}/\Delta t$.

High-quality μPIV analysis with good statistics is achieved by repetitive measurements and subsequent averaging of the correlation function C, a procedure known as correlation average. In this work, all acoustophoretic focusing experiments were repeated between 25 and 100 times. For the procedure to work best, it is imperative to avoid both clustering and depletion of tracer particles.[30] The following procedure was adopted: In a given time-sequence of image frames recorded immediately after the onset of ultrasound, the first frame was discarded to ensure that the acoustic resonance was fully developed; only the second and third frame was analyzed, as the particle distribution rapidly becomes inhomogeneous due to the acoustophoretic force potential. Furthermore, better statistics and sub-pixel resolution was obtained by using an iterative window shifting algorithm based on a smoothed continuum version of the discrete correlation function.[31] Finally, the accuracy of the analysis was refined by use of a central difference interrogation window method and a four-point image correction.[26]

The μPIV analysis was carried out using the software *EDPIV - Evaluation Software for Digital Particle Image Velocimetry* (http://www.edpiv.com). As part of the analysis, the recorded bright-field images were inverted and the background was subtracted. The background was derived by finding the lowest pixel intensity in the whole data set for each pixel position. To ensure convergence of the μPIV algorithm 20 window-shifting iterations was employed. Unless otherwise stated, the interrogation window size $S \times S$ was set to $S = 64$ pixel, and we used a 50% overlap such that the side length in the square grid (x_n, y_m) of Fig. 1 is $S/2 = 32$ pixel. Search radius for the shift-vector $\Delta \boldsymbol{r}$ was set to 20 pixel.

The μPIV results for the acoustophoretic velocity field was validated by particle tracking velocimetry (PTV), see Section IV E. In PTV, a set of tracer particles are identified manually in the first frame and then tracked throughout the subsequent (long) sequence of frames. The tracking is achieved by extraction of a sub-image containing the particle, which is thereafter cross-correlated with a small region in its vicinity in the succeeding frame. Generally, PTV has poor precision, but it is accurate, which can easily be verified by overlaying the acquired tracks with the analyzed frames.

C. Discrete acoustophoretic velocity field

From the μPIV analysis we obtain the acoustophoretic velocity field of the tracer particles

$$\boldsymbol{u} = \boldsymbol{u}(x_n, y_m) = \begin{pmatrix} u_x(x_n, y_m) \\ u_y(x_n, y_m) \end{pmatrix} \quad (5)$$

on the discrete lattice (x_n, y_m) with indices $1 \le n \le N$ and $1 \le m \le M$, see Fig. 1. The rectangular lattice has the lengths $L_x = x_N$ and $L_y = y_M$ along the x- and y-direction, respectively. For quantitative comparisons of acoustophoretic velocity fields $\boldsymbol{u}$, we use both the local speed $u(x_n, y_m) = |\boldsymbol{u}(x_n, y_m)|$ and the L^2-norm $\|\boldsymbol{u}\|$. The (square of the) latter is defined as

$$\|\boldsymbol{u}\|^2 = \frac{1}{NM} \sum_{n=1}^{N} \sum_{m=1}^{M} \left|\boldsymbol{u}(x_n, y_m)\right|^2. \quad (6)$$

Note that $\|\boldsymbol{u}\|$ can be thought of as an area-average speed, while $\|\boldsymbol{u} - \boldsymbol{u}_0\|^2$ is the variance of $\boldsymbol{u}$ around $\boldsymbol{u}_0$.

III. Chip, setup, and experimental procedure

A. Chip and experimental setup

Acoustophoresis microfluidic chip. A chip was fabricated with similar design as previously examined in ref. 20. Briefly, the chip consists of a straight channel of length $L = 35$ mm, width $w = 377$ μm, and height $h = 157$ μm, KOH-etched in a ⟨100⟩ silicon wafer of thickness $h_{\mathrm{si}} = 350$ μm. The channel was sealed by an anodically bonded pyrex lid of thickness $h_{\mathrm{py}} = 1.13$ mm. The chip length equals the channel length L and the chip width is $W = 2.52$ mm. To interface the channel, pieces of silicone tubing were glued to the chip inlet and outlet at each end, oriented along the channel axis, see Fig. 2.

Chip assembly. To achieve good long term stability, all parts of the chip assembly were glued together using ethyl-2-cyanoacrylat (ExpressLim, Akzo Nobel Bygglim AB, Sweden). From bottom and up sandwiched together: an aluminum mounting plate also serving as heat sink, a Peltier element (40 mm × 40 mm), an

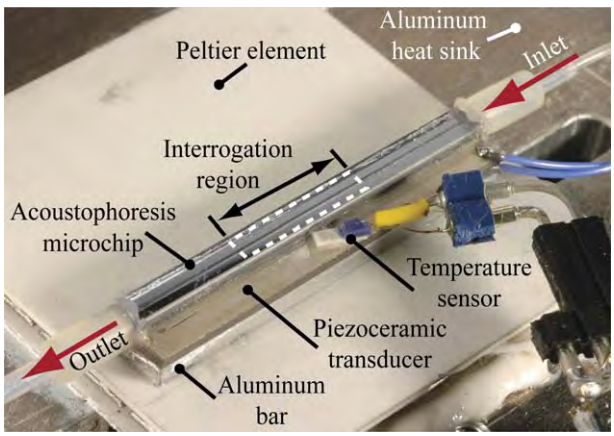

Fig. 2 Photograph of the acoustophoresis microchannel. The chip, piezo transducer (PZT), aluminum bar and Peltier element were sandwiched and glued together on a microscope stage. A Pt100 thermoresistive element was glued onto the PZT for feedback to the temperature control loop.

aluminum bar (35 mm × 5 mm × 1.5 mm), a piezo transducer (PZT) (35 mm × 5 mm × 1 mm, PZT26, Ferroperm Piezoceramics, Denmark), and the acoustophoresis chip, see Fig. 2. A Pt100 thermo-resistive element for temperature measurement was glued onto the PZT alongside the acoustophoresis chip, see Fig. 2.

Acoustics driving electronics. The PZT was driven by a function generator (33120A, Agilent Technologies Inc., Santa Clara, CA, USA) at a frequency f in the 2-MHz-range *via* a power amplifier circuit (LT1210, Linear Technologies Corp., Milpitas, CA, USA) configured with 10 Ω output impedance. The peak-to-peak voltage amplitude U_{pp} over the PZT was recorded with an oscilloscope (TDS 1002, Tektronix UK Ltd., Bracknell, UK). The onset of acoustic actuation was controlled by an external gate signal to the function generator.

Temperature control. Readings from the Pt100 element were recorded and temperature T was regulated using the Peltier element. A PID control loop was implemented on a computer interfaced by a data acquisition card (DAQ) (NI USB-6008, National instruments, Austin, TX, USA) and complementary circuits for generating constant current for 4-wire temperature measurement and for power amplification of the Peltier drive.

External fluidics. A syringe pump (neMESYS, Cetoni GmbH, Korbussen, Germany) and a motorized 2-position 4-way diagonal valve (V101, Upchurch Scientific, Oak Harbor, WA, USA), was interfaced to the computer. When the valve is in its initial position, microbead suspension can be withdrawn from a test tube into a 1-mL syringe (1001 LT, Hamilton Bonaduz AG, Bonaduz, Switzerland), while the inlet and outlet of the microchannel is short circuited, abruptly stopping flow in the channel. Switching the valve will connect the syringe with the chip inlet while the outlet will be open to the test tube. The configuration has two main advantages: microbeads can be reused for several passages through the microchannel, and repeated withdrawal and infusion of sample at high flow rates induces mixing in the test tube, preventing microbeads from sedimenting during long measurement series.

Imaging. A brightfield microscope (DM2500 M, Leica Microsystems CMS GmbH, Wetzlar, Germany) was equipped with a high-speed camera (EoSens mini MC-1370, Mikrotron GmbH, Unterschleissheim, Germany) set to an exposure time of 150 μs and frame rates ranging from 50 to 800 Hz. The image size is 1280 × 640 pixel corresponding to 0.88 mm × 0.44 mm in object plane (*i.e.* 1 pixel ∼ 0.69 μm). The image of a 5-μm-diameter tracer particle is thus ∼ 7 × 7 pixel. The camera is trigged by an external signal that is also the gate signal for the onset of ultrasound. For each trig, the camera records a predetermined number of images that are stored in an on board memory. The memory can store a maximum of 2500 images which has to be accounted for when setting up experimental series of multiple repeats. The frame rate of the camera can be set by the computer software by an external synchronization signal from a GPIB interfaced function generator.

Spatial positioning. To assess the global behavior of the acoustic resonances, image sequences must be captured from multiple positions along the channel. To be able to reliably stitch together the recorded velocity fields, accurate and reproducible positioning of the chip mount is important. Spatial positioning was controlled *via* a motorized *xyz*-stage (MTmot, Märzhäuser Wetzlar GmbH, Wetzlar, Germany). Positions were chosen with a 10% overlap between images. Overlapping areas would thereby be analyzed twice providing a measure of the discrepancy between adjacent fields of view.

Control software. A LabView program was developed, dedicated for controlling the experimental sequence. Its primary functionality is to regulate temperature in a PID-loop and to create a gate signal to the system to actuate ultrasound and trig the camera. A list of settings specifies ultrasound frequency and amplitude, camera frame rate and oscilloscope measurement range. For each onset of ultrasound, voltage over the PZT is recorded and stored *via* the GPIB interfaced oscilloscope. The program also controls the syringe pump and the motorized valve which enables the program to complete a whole sequence of experiments with different settings, each repeated a specified number of times. The experimental setup is sketched in Fig. 3.

B. Experimental procedures

In general, various aspects of acoustophoretic focusing were measured in stop-flow mode using an aqueous suspension of polystyrene microbeads (3 g L^{-1}, diameter $d = (5.16 \pm 0.08)$ μm, Sigma-Aldrich) with the addition of the surfactant Tween20 (0.01%, Sigma-Aldrich). The particle concentration is kept low to diminish particle–particle interactions and ensuring the validity of the single-particle theory presented in Section II A. Prior to each experiment 1 mL of this suspension was loaded into the system, and the *xyz*-stage position and the microscope focal plane were calibrated.

A given experiment was specified in the control software by the following list of settings: ultrasound frequency and amplitude, oscilloscope measurement range, camera frame rate, temperature set point, ultrasound gate time, temperature settling time, and number of repeats. Once initiated, the software automatically executes the timing of events for each individual acoustophoretic focusing experiment throughout the experimental series in the following order, Fig. 3(e):

1. The valve is switched to position I, Fig. 3(c), and 500 μL of bead suspension is withdrawn from the test tube into the syringe.
2. The valve is switched to position II, Fig. 3(d), and 100 μL of bead suspension is injected through the chip at 33 μL s^{-1} into the test tube.
3. The valve is switched back to position I to stop the flow in the microchannel, and the remaining bead suspension is emptied at a flow rate of 100 μL s^{-1} into the test tube to induce mixing.
4. The system is idle for a time of ∼ 10 s to allow for the temperature to stabilize to within ± 0.1 °C of the preset value.
5. A gate signal activates ultrasound for ∼ 100 ms and triggers the camera to capture a predefined number of frames.
6. The PZT voltage amplitude U_{pp} is registered *via* the oscilloscope. It has an uncertainty of 5%.

The system automatically closes down at the end of a complete experimental series.

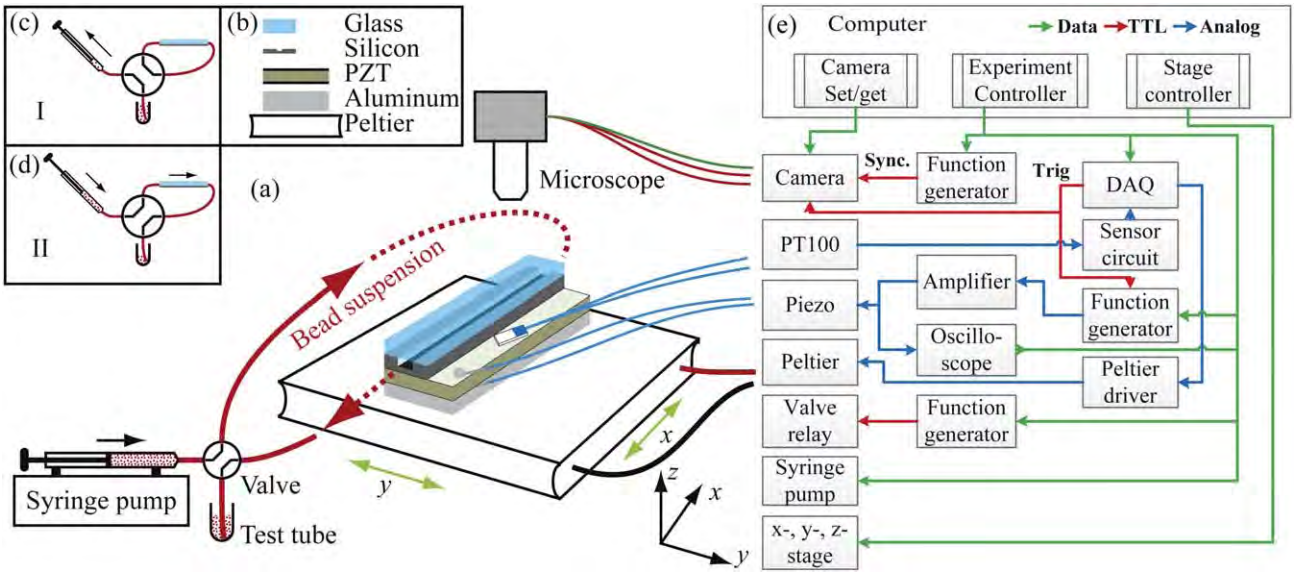

Fig. 3 (a) Schematic of the automated, temperature-controlled acoustophoresis μPIV setup. (b) The chip, PZT, aluminum slab, and Peltier element were sandwiched and glued together, resting on the microscope stage. (c) The valve in position *I* stops the flow in the chip, and the particle suspension can be transferred between syringe and test tube. (d) The valve in position *II* allows for injecting the particle suspension into the channel and redirecting it back into the test tube for reuse. (e) Diagram of the software and hardware configuration controlling the temperature and experimental timing sequence, positioning of the channel, and the camera setup.

The above procedure was employed to carry out the following eight types of experiments reported in this work:

1. The global spatial structure of the three resonance modes at $f = 1.940$ MHz, 1.951 MHz, and 1.968 MHz in a 12 mm long section of the microchannel at $T = 25$ °C, see Section IV A.
2. Optimization of μPIV settings: image-pair time-shift and standard deviation of velocities, see Section IV B.
3. Optimization of μPIV settings: window size S in the range 16 to 128 pixel, and image pair number $n_{\mathrm{tot}}^{\mathrm{pair}}$ in the range 1 to 100, see Section IV C.
4. The scaling of the acoustophoretic velocity with the PZT-voltage U_{pp} to the power 2, see Section IV D.
5. Comparison of μPIV with PTV, see Section IV E.
6. Temperature stability toggling between $T = 20$ °C and 25 °C for the fixed frequency $f = 1.963$ MHz and driving voltage $U_{\mathrm{pp}} = 1.8$ V, see Section V A.
7. Temperature sensitivity during frequency scans from $f = 1.931$ MHz to 1.980 MHz in steps of 1 kHz at $T = 23$ °C, 25 °C, and 27 °C for $U_{\mathrm{pp}} = 2.0$ V, see Section V B.
8. The focusing efficiency in continuous-flow mode correlated with the resonance modes measured by μPIV in stop-flow mode, see Section VI.

IV. Evaluation of the μPIV analysis

The results section begins with an evaluation of the μPIV analysis and a description of how appropriate settings of the μPIV parameters were chosen. The spatial inhomogeneity of the resonant modes results in inhomogeneous acoustophoretic velocity fields with a large dynamic range, which hurdles the accuracy of the μPIV analysis. To obtain good results, μPIV-parameters were optimized by analyzing the standard deviation of the velocity fields.

A. Global spatial structure of the resonance modes

The capability of the automated μPIV system is illustrated in Fig. 4. Here, the result of high-resolution measurements of the global spatial structure of the acoustic resonance modes ($f = 1.940$ MHz, 1.951 MHz, and 1.968 MHz determined as described in Section V B) is shown for a 12-mm-long section at the center of the 35-mm-long microchannel, Fig. 4(a). The color plots in Fig. 4 (b) show the speed u/u_{max} of the acoustophoretic velocity fields for the 5-μm-diameter polystyrene tracer particles normalized by the maximum speed u_{max}. For each frequency a total of 15 adjacent image frames were stitched together with an overlap of 10%, and the acoustophoretic focus experiment was repeated 25 times for each position of the image frame. For all measurements the temperature was kept constant at 25 °C.

To accommodate for the high dynamic range in the acoustophoretic velocity of the tracer particles, the cameras frame rate was set to either 400 Hz or 800 Hz. To achieve the same microbead displacement for each of the three frequencies as described in Section IV B, the driving voltage was set to $U_{\mathrm{pp}} = 2.00$ V at $f = 1.940$ MHz, 1.25 V at 1.951 MHz, and 0.75 V at 1.968 MHz. The interrogation window size was $S = 64$ pixel leading to a grid size of 32 pixel and thus a grid resolution of 22 μm.

In Fig. 4(c) more details in the spatial structure of the resonances are made visible by color plots of $\log(u/u_{\mathrm{max}})$. This is particularly evident for $f = 1.968$ MHz, where four local maxima become visible.

B. Image-pair time-shift and standard deviation

The uncertainty in terms of standard deviation in the velocity fields obtained by μPIV was minimized by optimizing three parameters: the displacement of the tracer particles between the

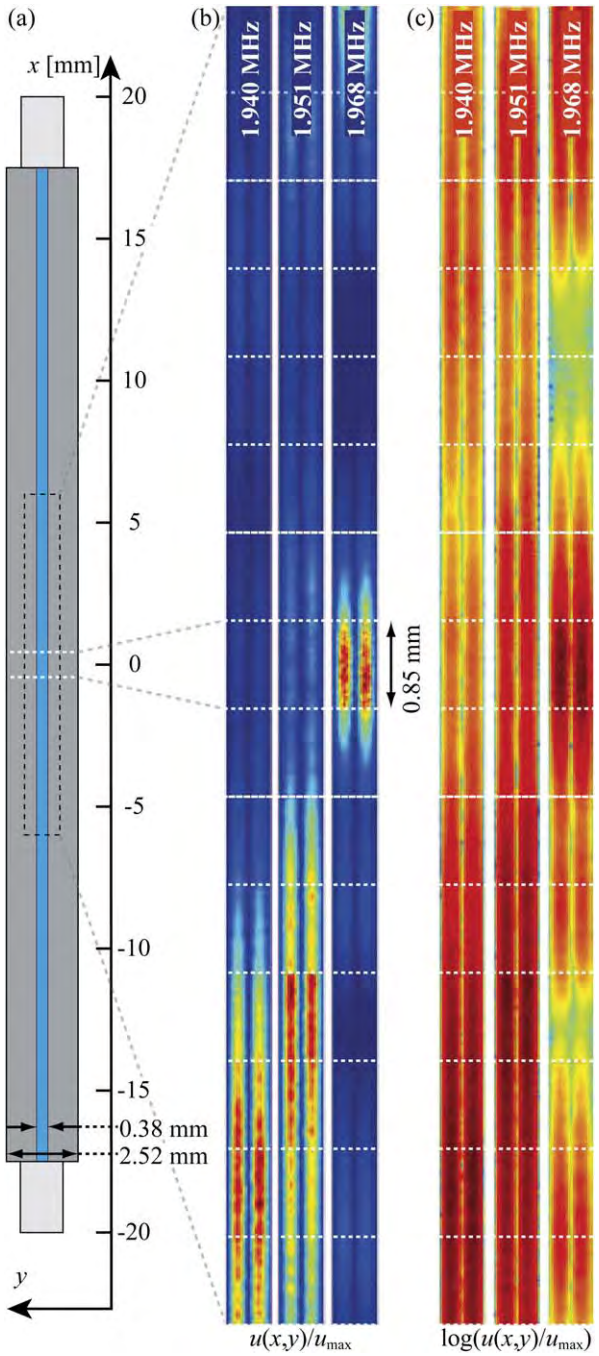

Fig. 4 Global spatial structure of three acoustic resonance modes. (a) Schematic of the chip indicating the 12-mm-long section investigated. The white lines represent the channel-center single-image frame used in Secs. IV and V. (b) Color plot from 0 (dark blue) to 1 (dark red) of the normalized acoustophoretic speed $u(x, y)/u_{max}$ measured by μPIV at $T =$ 25 °C for the three resonance frequencies $f = 1.940$ MHz, 1.951 MHz, and 1.968 MHz. For other experimental parameters see Section IV.A. The data consist of 25 repetitions in 15 stitched image frames per frequency (white lines), and the acquisition took 3 days. (c) Color plot of the natural logarithm of $u(x, y)/u_{max}$ from panel (b).

two images in an image pair, the number of repeated measurements, and the size S of the interrogation window.

In μPIV the best results are obtained if the maximum displacement of the tracer particles within an image pair is about one to a few times the diameter of the particles. To verify this, the image frame was positioned in the channel center as indicated in Fig. 4(a), with $T = 25$ °C, $f = 1.968$ MHz, and $U_{pp} = 2.95$ V. Then 100 repeats of the acoustophoretic focusing were recorded, capturing 10 time frames per repeat at a frame rate of 800 Hz. From the data, nine different μPIV image pairs can be constructed by pairing frame 1 with frame $1 + n$ (for $n = 1, 2, \ldots, 9$), and this leads to the nine possible time shifts $\Delta t = n \times 1.25$ ms, see eqn (4).

The maximum acoustophoretic velocity in this experiment was measured to be 1 mm s^{-1} corresponding to a maximum particle displacement of $n \times 1.8$ pixel for the nine different image-pair time shifts. In Fig. 5(a) we plot the normalized area-average acoustophoretic speed $\|\boldsymbol{u}\|$ as a function of this maximum pixel displacement. A distinct maximum is seen around 7 pixel corresponding to the tracer-particle diameter of 5 μm. In all of the μPIV analysis the PZT voltage U_{pp} was therefore set to achieve this displacement as accurate as possible.

The image-pair time-shift is only one of many parameters of the μPIV analysis we need to optimize. In practice, the determination the acoustophoretic velocity field is a trade-off between the desired velocity accuracy and the time it takes to carry out the experiment and μPIV analysis. For a given microbead concentration, a certain velocity accuracy requires a minimum number of uncorrelated image pairs n_{tot}^{pair} and a maximum interrogation window size $S \times S$. If the interrogation window size is too large, the resolution of the velocity field is too low to resolve the dynamics, but the smaller the window gets, the more experimental repetitions n_{tot}^{pair} are needed to ensure a proper bead coverage and thus sufficient statistics in

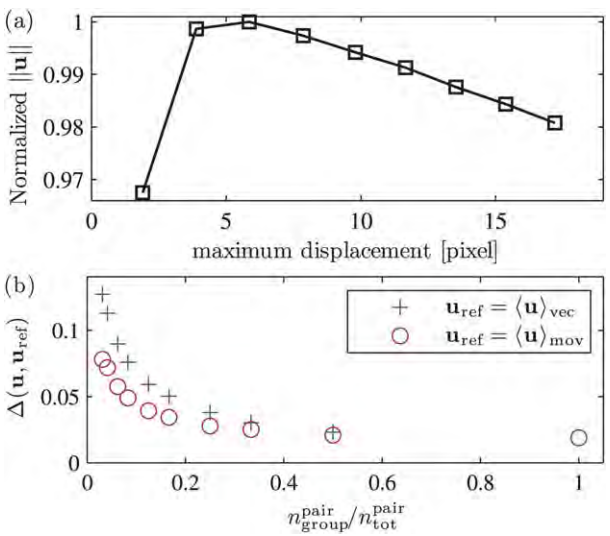

Fig. 5 (a) Area-average acoustophoretic speed $\|\boldsymbol{u}\|$ *versus* maximum particle displacement within the channel-center single-image frame using $n_{tot}^{pair} = 100$ and $S = 32$ pixel. (b) The relative standard deviation $\Delta(\boldsymbol{u}, \boldsymbol{u}_{ref})$ of the acoustophoretic velocity field $\boldsymbol{u}$ with $u_{max} = 0.8$ mm s^{-1} determined by μPIV as function of the amount $n_{group}^{pair}/n_{tot}^{pair}$ of correlation averaging for integer division of $n_{tot}^{pair} = 96$. For u_{ref} is used either the vector average $\langle \boldsymbol{u} \rangle_{vec}$ (blue +) or the moving average $\langle \boldsymbol{u} \rangle_{mov}$ (red ○), see eqn (7).

the μPIV analysis. Therefore, it is important to carry out a parametric study of the μPIV analysis settings and number of experimental repetitions for a certain set of experimental parameters, such as microbead concentration, camera frame rate, and microbead velocities.

One way to estimate the standard deviation on an acoustophoretic velocity field determined by μPIV is to repeat a given image-pair measurement $n_{\mathrm{tot}}^{\mathrm{pair}}$ times, and then sub-divide this series into N_{group} groups each containing $n_{\mathrm{group}}^{\mathrm{pair}}$ image pairs ($n_{\mathrm{group}}^{\mathrm{pair}} = N_{\mathrm{group}} \times n_{\mathrm{group}}^{\mathrm{pair}}$). For each group a μPIV analysis involving averaging over the $n_{\mathrm{group}}^{\mathrm{pair}}$ cross-correlation functions is performed resulting in N_{group} velocity fields $\boldsymbol{u}_i$. The vector average $\langle u \rangle_{\mathrm{vec}} = \sum_{i=1}^{N_{\mathrm{group}}} u_i / N_{\mathrm{group}}$ is calculated, and the relative standard deviation $\Delta(\boldsymbol{u}, \boldsymbol{u}_{\mathrm{ref}})$ of $\boldsymbol{u}$ around the reference field $\boldsymbol{u}_{\mathrm{ref}} = \langle \boldsymbol{u} \rangle_{\mathrm{vec}}$ can be estimated from the variance $\|\boldsymbol{u} - \boldsymbol{u}_{\mathrm{ref}}\|^2$, see eqn (9), and the maximum speed $u_{\max}$ of $\boldsymbol{u}$, as

$$\Delta\left(\boldsymbol{u}, \boldsymbol{u}_{\mathrm{ref}}\right) = \sqrt{\frac{1}{N_{\mathrm{group}}} \sum_{i=1}^{N_{\mathrm{group}}} \frac{\|\boldsymbol{u}_i - \boldsymbol{u}_{\mathrm{ref}}\|^2}{u_{\max}^2}}. \qquad (7)$$

In Fig. 5(b) is shown the result of this vector-average estimate (blue +) of the relative standard deviation $\Delta(\boldsymbol{u}, \langle \boldsymbol{u} \rangle_{\mathrm{vec}})$ *versus* for $n_{\mathrm{tot}}^{\mathrm{pair}} = 96$. In the limit where the sub-groups contains a single image pair ($n_{\mathrm{tot}}^{\mathrm{pair}} = 1$) each of which leads to a μPIV velocity field by a single cross-correlation function eqn (7), the method corresponds to pure vector averaging of the resulting $N_{\mathrm{group}} = n_{\mathrm{tot}}^{\mathrm{pair}} = 96$ velocity vector fields. In the opposite limit ($n_{\mathrm{group}}^{\mathrm{pair}} = n_{\mathrm{tot}}^{\mathrm{pair}}$), the average of the correlation functions of all 96 image pairs is used to calculate a single μPIV velocity field ($N_{\mathrm{group}} = 1$), and the method corresponds to pure correlation function averaging. For intermediate values $1/96 < n_{\mathrm{group}}^{\mathrm{pair}}/n_{\mathrm{tot}}^{\mathrm{pair}} < 1$, the method is a combination of vector averaging and correlation averaging. In Fig. 5(b) it is seen that for the given 96 image pairs, $\Delta(\boldsymbol{u}, \langle \boldsymbol{u} \rangle_{\mathrm{vec}})$ decreases monotonically from 12% for $n_{\mathrm{group}}^{\mathrm{pair}}/n_{\mathrm{tot}}^{\mathrm{pair}} = 0.01$ to below 3% for $n_{\mathrm{group}}^{\mathrm{pair}}/n_{\mathrm{tot}}^{\mathrm{pair}} = 0.5$ supporting the fact[27] that correlation average yields better precision in μPIV than vector average. Although viable, the vector-averaging method is a time-consuming way (24 h to obtain the results for $\Delta(\boldsymbol{u}, \langle \boldsymbol{u} \rangle_{\mathrm{vec}})$ to obtain the standard deviation as it requires additional μPIV analysis and additional number of experimental repeats. A more efficient way is to use the 3-by-3-point moving-average method, where $\Delta(\boldsymbol{u}, \boldsymbol{u}_{\mathrm{ref}})$ is calculated using for each point (x_n, y_m) in the grid the nearest-neighbor average $\boldsymbol{u}_{\mathrm{ref}}(x_n, y_m) = \langle \boldsymbol{u} \rangle_{\mathrm{mov}}(x_n, y_m)$ of the velocity $\boldsymbol{u}_i$ of the 3×3 points having (x_n, y_m) in the center. It is seen in Fig. 5(b) that the moving-average estimate $\Delta(\boldsymbol{u}, \langle \boldsymbol{u} \rangle_{\mathrm{mov}})$ (red ○) agrees well with the vector-average method, settling around 2% for $n_{\mathrm{group}}^{\mathrm{pair}}/n_{\mathrm{tot}}^{\mathrm{pair}} = 1$. No additional effort is needed when using the moving-average method and thus it is used in the rest of the paper to evaluate the standard deviation $\Delta(\boldsymbol{u}, \boldsymbol{u}_{\mathrm{ref}})$.

Another test of the accuracy of the μPIV measurements is to measure the velocity in the case of no acoustical drive, *i.e.* for $U_{\mathrm{pp}} = 0$. The obtained area-averaged speed is $\|\boldsymbol{u}\| = 7.3\ \mu\mathrm{m\ s}^{-1}$, which primarily stems from the x-component, indicative of a small drift even though the flow is stopped. Thus, the velocity magnitude cannot be expected to be determined more accurately than this. For resonant modes typically $\|\boldsymbol{u}\| \approx 500\ \mu\mathrm{m\ s}^{-1}$, thus the accuracy cannot be better than $\sim 2\%$.

In conclusion, using the μPIV settings described above, our automated system is routinely capable of obtaining acoustophoretic velocity fields with a spatial resolution of about 20 μm with an uncertainty of $\sim$ 5%. Higher resolution and lower uncertainty can be obtained by going beyond 100 repeats per focus experiment.

C. Window size and number of image pairs

The next step is to investigate how the quality of the μPIV results depends on the number $n_{\mathrm{tot}}^{\mathrm{pair}}$ of uncorrelated image pairs (number of repeats) and the pixel size S of the quadratic $S \times S$ interrogation window. Other more detailed studies of additional μPIV parameters such as the search radius, number of window shifting iterations, and various central-difference schemes are not treated here.

In Fig. 6(a) is shown plots of the relative standard deviation $\Delta(\boldsymbol{u}, \boldsymbol{u}_{\mathrm{ref}})$ of the velocity field $\boldsymbol{u}$ as a function of $n_{\mathrm{tot}}^{\mathrm{pair}}$ and S using the moving-average method $\boldsymbol{u}_{\mathrm{ref}} = \langle \boldsymbol{u} \rangle_{\mathrm{mov}}$ with $n_{\mathrm{group}}^{\mathrm{pair}} = n_{\mathrm{tot}}^{\mathrm{pair}}$ and $N_{\mathrm{group}} = 1$. As the number of uncorrelated image pairs $n_{\mathrm{tot}}^{\mathrm{pair}}$ increases, $\Delta(\boldsymbol{u}, \langle \boldsymbol{u} \rangle_{\mathrm{mov}})$ decreases. The high uncertainty $\sim 10\%$ for $S = 128$ pixel is also visible in the line and color plots of the speed u in panel (b) and (c), respectively. The effect of the low tracer particle concentration used, is reflected in the observation that the lowest standard deviation is obtained for $S = 32$ pixel. For the smallest interrogation window size $S = 16$ pixel the number of tracer particles per window is so low that the statistical fluctuations increase noticeably, compare 16 pixel and 32 pixel in panel (c). The relative standard deviation for $S = 32$ pixel drops below 3% already for $n_{\mathrm{tot}}^{\mathrm{pair}} = 20$. This tendency is supported by the plot of $\Delta(\boldsymbol{u}, \boldsymbol{u}_{\mathrm{ref}})$ using the velocity field $\boldsymbol{u}_{32}^{100}$ obtained for $S = 32$ pixel and $n_{\mathrm{tot}}^{\mathrm{pair}} = 100$ as $\boldsymbol{u}_{\mathrm{ref}}$ for all four values of S. This plot also shows that to obtain an uncertainty below 5% it is thus sufficient to use $n_{\mathrm{tot}}^{\mathrm{pair}} = 20$ and $S = 64$, so this we use in our application example in Section VI leading to a spatial resolution of 20 μm.

In Fig. 6(b) are shown two line plots of the speed $u(x_0, y)$ along the transverse y-direction at $x_0 = 223$ μm and $x_0 = 713$ μm with $n_{\mathrm{tot}}^{\mathrm{pair}} = 100$ for the same data as in panel (a). Except for the most coarse-grained resolution ($S = 128$ pixel), the other three window sizes $S = 64$ pixel, 32 pixel, and 16 pixel agree well. However, close to the wall both $S = 128$ pixel and 64 pixel differs from $S = 32$ pixel and 16 pixel, because the large window sizes results in a significant overlap of windows with the channel walls, which results in an erroneous contribution of non-zero velocities outside the channel.

In Fig. 6(c) are shown plots of the acoustophoretic velocity field $\boldsymbol{u}$ (arrows) and speed u (colors) corresponding to the data in Fig. 6(b) using $n_{\mathrm{tot}}^{\mathrm{pair}} = 100$ and $S = 128$, 64, 32, and 16 pixel. The resolution clearly increases as S decreases, but simultaneously the noise increases because the number of tracer particles in each interrogation window decrease. In the color plots are marked the two x-coordinates, $x_0 = 223$ μm and $x_0 = 713$ μm corresponding to the two line plots in Fig. 6(b).

As observed, a lower standard deviation $\Delta(\boldsymbol{u}, \boldsymbol{u}_{\mathrm{ref}})$ can be obtained by increasing $n_{\mathrm{tot}}^{\mathrm{pair}}$. However, the cost is an increased time t^* for data acquisition and analysis: $t^* = (\tilde{t}_{\mathrm{exp}} + \tilde{t}_{\mathrm{img}} + \tilde{t}_{\mathrm{PIV}}) n_{\mathrm{tot}}^{\mathrm{pair}}$, where $\tilde{t}_{\mathrm{exp}}$ is the measurement time per image pair, $\tilde{t}_{\mathrm{img}}$ the image analysis time per image pair, and $\tilde{t}_{\mathrm{PIV}}$ the time for the total μPIV analysis per image pair. Rough estimates of the times per image

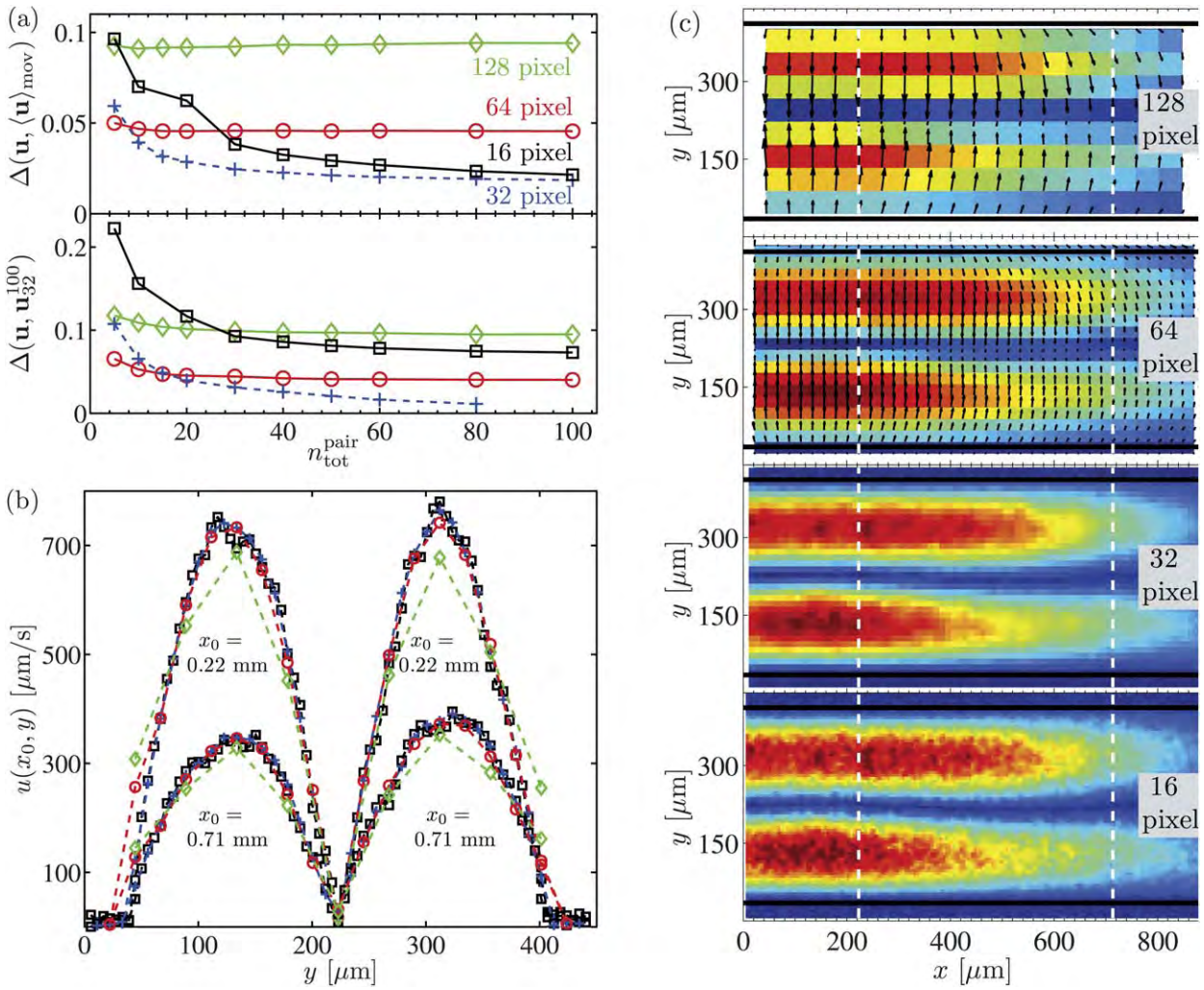

Fig. 6 The μPIV acoustophoretic velocity fields ($T = 25\,^{\circ}\mathrm{C}, f = 1.968$ MHz, $U_{pp} = 1.89$ V) in the channel-center single-image frame of Fig. 4 *versus* the number n_{tot}^{pair} of uncorrelated image pairs and of the interrogation window size S. (a) The relative deviation $\Delta(\boldsymbol{u}, \boldsymbol{u}_{ref})$ of the velocity u relative to the reference velocity fields $\langle \boldsymbol{u} \rangle_{mov}$ (moving average field) and u_{32}^{100} ($S = 32$ pixel and $n_{tot}^{pair} = 100$) as a function of n_{tot}^{pair} (from 1 to 100) and S [128 pixel (green ◇), 64 pixel (red ○), 32 pixel (blue +), and 16 pixel (black □]. (b) Two line plots of the speed $u(x_0, y)$ along the transverse y-direction at $x_0 = 223$ μm and $x_0 = 713$ μm with $n_{tot}^{pair} = 100$ for the same data as the previous panel. (c) Acoustophoretic velocity fields (arrow plots) and speed fields (color plots, from 0 μm s^{-1} (dark blue) to 800 μm s^{-1} (dark red)) for the same data as the previous panel. From top to bottom panel the window size is $S = 128$ pixel, 64 pixel, 32 pixel, and 16 pixel. The white dashed lines indicate the two line plots in panel (b).

pair are $\tilde{t}_{exp} \sim 30$ s, $\tilde{t}_{img} \sim 20$ s, and $\tilde{t}_{PIV} \sim 60$ s, which for $n_{tot}^{pair} = 20$ results in a total time $t^* \sim 30$ min to run one set of parameters.

D. Frame rate and voltage dependence

The PZT driving voltage U_{pp} appears in the acoustic responses as $p_a \propto U_{pp}$ and $u_y \propto U_{pp}^2$. The latter is clear from eqn (3c) and the fact that $E_{ac} \propto p_a^2$. Therefore, U_{pp} has a decisive influence of which frame rate to choose for the μPIV analysis. The dependence of the acoustophoretic velocity u on U_{pp} was evaluated for the three frequencies $f = 1.940$ MHz, 1.951 MHz, and 1.968 MHz, each identified as a local maximum of u in the recorded frequency spectrum at $T = 25\,^{\circ}\mathrm{C}$. The maximum allowed driving voltage U_{pp}^{max} was limited by the maximum camera frame rate of 800 Hz at the chosen image size. For each frequency, U_{pp}^{max} was adjusted to obtain the optimal tracer particle displacement shown in Fig. 5(a), and then the acoustophoretic velocity field was acquired for seven driving voltages ranging from zero to U_{pp}^{max}.

From the analyses of the three resonance frequencies it was verified that the acoustophoretic velocity scales by U_{pp} to the power of 2. For each frequency, the measured data points $\|\boldsymbol{u}\|$ were fitted to a power law $(U_{pp})^{\alpha}$ resulting in $\alpha = 1.7$, 2.1 and 2.0, respectively (data not shown). Fitting instead the measured maximum speed u_{max} yielded the same behavior with a distribution of the power ranging from 1.87 to 2.09. These results agree well with the findings in ref. [20].

E. Comparing μPIV with particle tracking

The μPIV analysis of the acoustophoretic velocity field was validated further by comparing estimates of the one-dimensional acoustic energy density E_{ac} obtained by the μPIV method developed in this work to our previously reported particle tracking method developed in ref. 20. This comparison is carried

out for the resonance mode at $f = 1.968$ MHz at $T = 25\,^{\circ}\mathrm{C}$, which is nearly a straight 1D resonance within the channel-center single-image frame of Fig. 4.

By μPIV analysis with $n_{\mathrm{tot}}^{\mathrm{pair}} = 100$ we obtained the acoustophoretic velocity field $\boldsymbol{u}(x, y)$, the magnitude of which is shown as the color plot in Fig. 7(a). As it is a nearly perfect 1D transverse standing wave, it is meaningful to calculate the x-direction-average $\langle u_y \rangle_x$ of the y-component u_y of $\boldsymbol{u}(x, y)$,

$$\langle u_y \rangle_x = \frac{1}{N} \sum_{n=1}^{N} u_y(x_n, y_m), \tag{8}$$

which is a function of the transverse grid coordinate y_m. In Fig. 7 (b), the analytical expression (4) for $u_y(y)$ (blue dashed line) is fitted to the values at y_m of $\langle u_y \rangle_x$ (red circles) using the acoustic energy density E_{ac} and half wavelength $\lambda/2$ as fitting parameters. The fit is good and results in $E_{\mathrm{ac}} = (98.0 \pm 1.1)$ J m^{-3} and $\lambda_y/2 = (374.0 \pm 1.5)$ μm, where the latter is close to the channel width $w = 377$ μm.

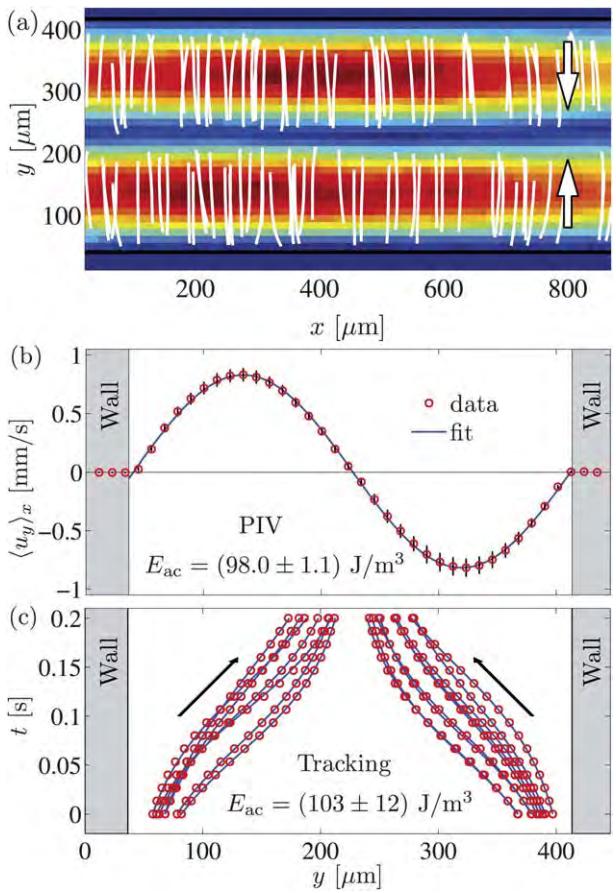

Fig. 7 (a) Acoustophoretic velocity field $\boldsymbol{u}(x, y)$ (arrow plot) and its magnitude (color plot from 0 μm s^{-1} (dark blue) to 900 μm s^{-1} (dark red)) at the channel center for temperature $T = 25\,^{\circ}\mathrm{C}$, driving frequency $f = 1.968$ MHz, and driving voltage $U_{\mathrm{pp}} = 1.89$ V. Also shown are 100 particle tracks (white) used to extract the acoustic energy density E_{ac} by the tracking method.[20] (b) Plot of the x-averaged y-component $\langle u_y \rangle_x$ (data: red circles; fit: blue line, standard deviations: black lines) of the acoustophoretic velocity field shown in panel (a). (c) Plot of the transverse path $y(t)$ (red circles, only every second data point is shown) and corresponding fit (eqn (5), blue lines) for 16 of the 100 microbead tracks.

To perform particle tracking, 10 additional focus experiments with the same settings as above were carried out. From these, the transverse $y(t)$ component of 100 particle tracks were extracted, see white lines in Fig. 7(a). Using our previously developed method ref. 20, each particle track was fitted to eqn (5) for $y(t)$, and E_{ac} and $\lambda_y/2$ were extracted as the fitting parameters leading to the acoustic energy density $E_{\mathrm{ac}} = (103 \pm 12)$ J m^{-3} and the half-wavelength $\lambda_y/2 = (382 \pm 27)$ μm. In Fig. 7(c) are shown 16 of the 100 tracks including the fitting curves.

The resonance parameters determined independently from the μPIV method and the particle tracking method are in good agreement with relative deviations less than 5%. We note that our new μPIV method allows for improved and faster statistics, and thus in general will lead to better results compared to the particle tracking method.

V. Stability and reproducibility of μPIV with temperature control

In the following we characterize the temperature control described in Section III A by performing stability and reproducibility tests *versus* frequency. In all the μPIV analyses we use $S = 64$ pixel and $n_{\mathrm{tot}}^{\mathrm{pair}} = 20$ repeats.

A. Fixed frequency

In order to obtain reliable data, the setup has to be state-dependent and reproducible without hysteresis effects. In Fig. 8 is shown a short-term temperature stability test, where the resonator temperature is toggled between 20 °C (panels (a) and (c)) and 25 °C (panels (b) and (d)) for the fixed frequency $f = 1.963$ MHz and driving voltage $U_{\mathrm{pp}} = 1.8$ V. The time between the experiments of same temperature is approximately two hours. The acoustophoretic velocity field $\boldsymbol{u}$ is indeed seen to be reliably state dependent on the resonator temperature with an relative error $\|\boldsymbol{u}_2 - \boldsymbol{u}_1\|/\|\boldsymbol{u}_1\| \approx 7\%$ between two measurements at the same temperature performed two hours apart.

B. Frequency scan

The temperature and frequency dependence of the acoustophoretic velocity was studied within the channel-center single-image frame for actuation frequencies in the range from 1.930 kHz to 1.980 kHz in steps of 1 kHz. The frequency spectrum was scanned at three constant temperatures $T = 23\,^{\circ}\mathrm{C}$, $25\,^{\circ}\mathrm{C}$, and $27\,^{\circ}\mathrm{C}$, and the spectrum at $25\,^{\circ}\mathrm{C}$ was re-evaluated two days later to validate the reproducibility of the system, see Fig. 9.

As described in Section 4.4, for each setting of f and T we tune the transducer voltage U_{pp} to a value leading to the optimum pixel displacement in the μPIV analysis shown in Fig. 5(a). In Fig. 9(a) we plot the measured values of U_{pp} *versus* frequency f for the three selected temperatures. Together with the U_{pp}-square scaling of the acoustophoretic velocity, we can use this curve to calibrate for the different voltage amplitudes at the different measurements. This calibration has been performed in Fig. 9(b), where we plot the normalized area-average speed $\left(\frac{1\mathrm{V}}{U_{\mathrm{pp}}}\right)^2 \|\boldsymbol{u}\|$, such that all values correspond to $U_{\mathrm{pp}} = 1$ V and the maximum value in the plot is unity (for $T = 27\,^{\circ}\mathrm{C}$ and $f = 1.967$ MHz). The

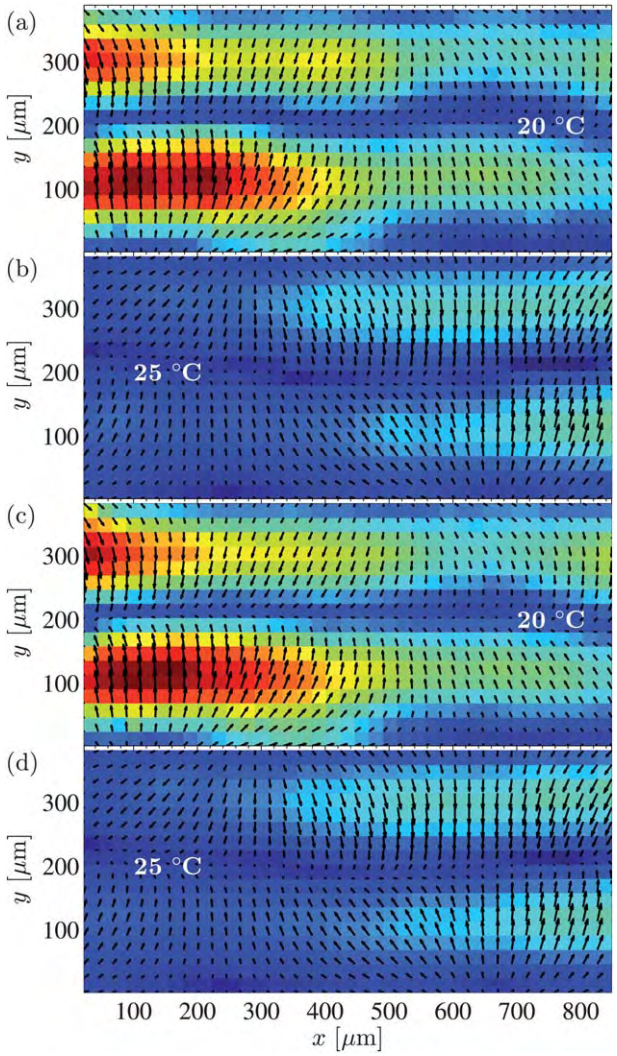

Fig. 8 Temperature stability of the experimental setup at $f = 1.963$ MHz and $U_{pp} = 1.8$ V illustrated by the acoustophoretic velocity field $\boldsymbol{u}(x_n, y_m)$ (arrows) and its magnitude $u(x_n, y_m)$ [color plot from 0 μm s^{-1} (dark blue) to 250 μm s^{-1} (dark red)] in four consecutive measurements at the channel-center single-image frame at temperature (a) $T = 20$ °C, (b) 25 °C, (c) 20 °C, and (d) 25 °C. The average relative error $\|\boldsymbol{u}_2 - \boldsymbol{u}_1\|/\|\boldsymbol{u}_1\| \approx 7\%$ between two measurements at the same temperature performed one hour apart.

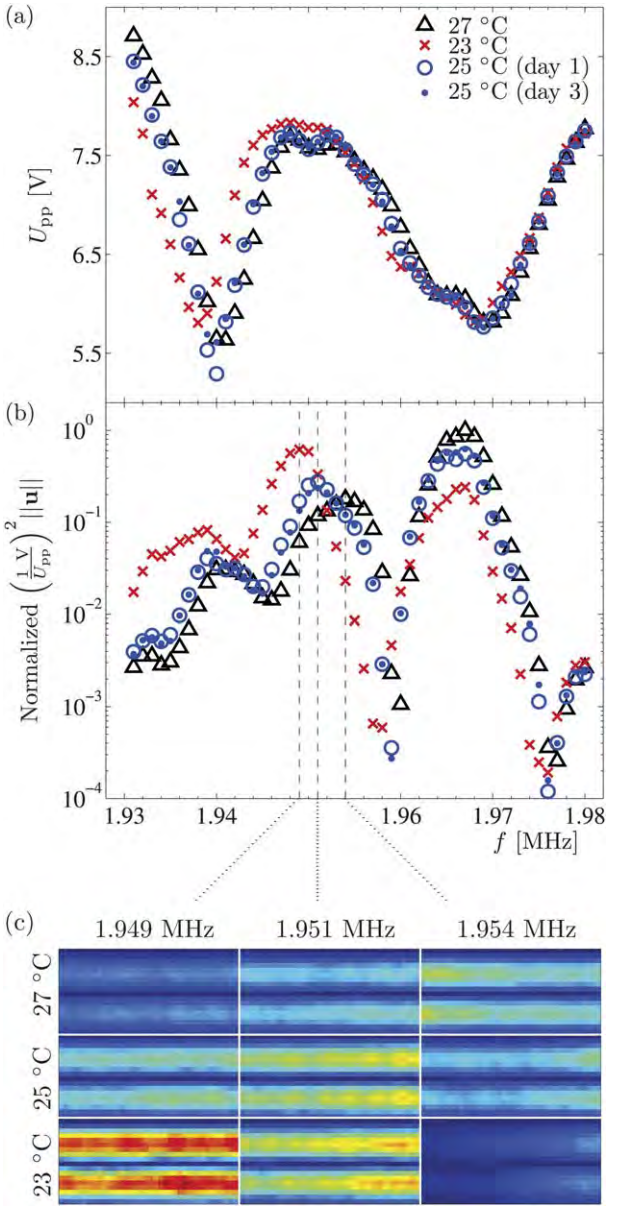

Fig. 9 Frequency dependence in the channel-center single-image frame. (a) The measured value of the transducer voltage U_{pp} *versus* frequency f used to maintain the particular maximum microbead velocity which leads to the optimal maximum pixel displacement in the μPIV analysis, see Fig. 5(a), at temperatures $T = 23$ °C (red ×), 25 °C (blue ○ for day 1, blue ● for day 3), and 27 °C (black Δ). (b) Semi-logarithmic plot of the area-averaged acoustophoretic speed $\left(\frac{1\,V}{U_{pp}}\right)^2 \|\boldsymbol{u}\|$ *versus* f normalized to unity at $f = 1.967$ MHz and $T = 27$ °C. All data points are calibrated to correspond to $U_{pp} = 1$ V by use of panel (a) and the $(U_{pp})^2$-dependence. (c) Color plot of the velocity magnitude (dark blue 0 mm s^{-1}, dark red 0.12 mm s^{-1}) normalized to $U_{pp} = 1$ V as in the previous panel for 3 × 3 temperature and frequency values near the 1.951-MHz resonance.

recording time of each spectrum is ~ 6 h, but in spite of this long time interval, the moving-average standard deviation $\Delta(\boldsymbol{u}, \langle \boldsymbol{u} \rangle_{mov})$ is only of the order of 5% (the size of the point symbols) in agreement with Fig. 5(b). Moreover, the relative difference between the day-1 and the day-3 spectrum at 25 °C is also only about 5%.

In the frequency dependence of $\|\boldsymbol{u}\|$, we observe three peaks at the frequencies $f = 1.940$ MHz, 1.951 MHz, and 1.968 MHz. Measuring the shift in Lorentzian peaks fitted to the data points, the temperature sensitivity $\Delta f/\Delta T$ of the resonance frequency of the 1.940-MHz-peak is found to be ≈ 1.25 kHz °C^{-1}, for the 1.951-MHz-peak ≈ 1.0 kHz °C^{-1}, and for the 1.968-MHz-peak ≈ 0.0 kHz °C^{-1}. These temperature-induced shifts of the resonance frequencies depend on the spatial distribution of the resonance mode in the full 3D structure of the system and the temperature coefficients of the system materials, and they are therefore difficult to determine, even using numerical simulation. However, the measured sensitivities are the right order of magnitude given the following estimates: If we assume that the entire mode is confined in the water, then from $f(T) = c_{wa}(T)/(2w)$ and the table values of $c_{wa}(T)$ we find $\Delta f/\Delta T \approx 3.5$ kHz °C^{-1}, while the sensitivity for

pyrex given $f(T) = c_{py}(T)/(2W)$ is $\Delta f/\Delta T \approx 0.1$ kHz °C^{-1} (for longitudinal waves).

C. Global spatial scan

After fixing the μPIV parameters using the above local analysis of the center-channel single-image frame, we now return to the global spatial scan of Fig. 4 for the three resonance frequencies $f = 1.940$ MHz, 1.951 MHz, and 1.968 MHz. A single frame is 0.85 mm long and thus only covers about 2.5% of the 35 mm long microchannel, whereas the 15 consecutive of Fig. 4(b) cover a length of 12 mm or about 34% of the microchannel.

It is striking that in this highly symmetric and very simple rectangular geometry with a horizontal inlet and outlet, we have succeeded in generating resonances, which in the 2D top-view appear as acoustophoretic velocity fields $\boldsymbol{u}$ with a mirror symmetry around the centerline in the transverse y-direction resulting in a nearly perfect straight line pressure nodal-line with $\boldsymbol{u} = \boldsymbol{0}$. However, equally clear are the strong variations along the channel axis (x-direction) in the measured $\boldsymbol{u}$-field. Despite the near-perfect geometry, the present data does not exhibit the sinusoidal axial pressure distribution in the resonance predicted by the idealized hard-wall model discussed in ref. 20. The reasons for this may be sought in the walls not being infinitely hard, the asymmetry due to the acoustical differences between the bottom silicon and top pyrex layer, the presence of inlet/outlet tubing, as well as imprecise mounting of the chip, the PZT, and the Peltier element.

To allow for quantitative comparisons between the three resonance modes, we do two things. First, we abandon the normalization used in Fig. 4(b), and instead use the absolute but voltage-calibrated, acoustophoretic velocities $\left(\frac{1\text{V}}{U_{pp}}\right)^2 \boldsymbol{u}$; and second, given the regular behavior in the transverse direction, we introduce the y-direction-average $\langle u \rangle_y$ of the speed $u(x_n, y_m)$,

$$\langle u \rangle_y = \frac{1}{M} \sum_{m=1}^{M} u(x_n, y_m), \tag{9}$$

which is a function of axial coordinate x_n.

In Fig. 10 we plot the voltage-corrected speed $\left(\frac{1\text{V}}{U_{pp}}\right)^2 \langle u \rangle_y$ *versus* axial position x for each of the three resonance frequencies at $T = 25$ °C. It is clear that globally the 1.940-MHz-mode (blue) leads to the highest acoustophoretic velocity, followed by 1.968 MHz (red), and 1.951 MHz (black) being lowest. Counting local maxima, the 1.940-MHz-mode (blue) has two peaks (at −4.8 mm and 3.6 mm), the 1.951-MHz-mode (black) three (at −2.8 mm, 0.8 mm and 4.6 mm), and the 1.968-MHz-mode (red) four (at −5.2 mm, −2.2 mm, 0 mm, and > 6 mm).

The global strengths of the resonance modes, expressed as the voltage corrected average transverse particle speed, can be characterized by the average $\sum(f) = \left(\frac{1\text{V}}{U_{pp}}\right)^2 \int_{\Omega} \langle u(f) \rangle_y \mathrm{d}x/(12\text{ mm})$, where Ω is the interval −6 mm < x < 6 mm. For the three modes we obtain Σ(1.940 MHz) = 51 μm s^{-1}, Σ(1.951 MHz) = 29 μm s^{-1}, and Σ(1.968 MHz) = 22 μm s^{-1}.

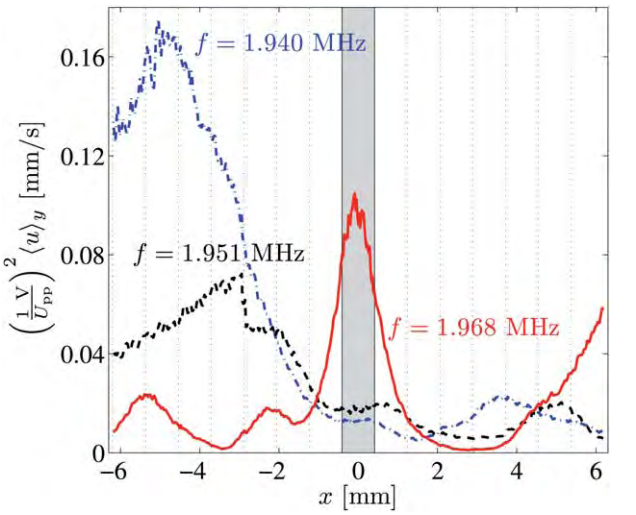

Fig. 10 The y-direction-average $\langle u \rangle_y$ of eqn (9) plotted as function of the axial position x along the 12-mm channel section shown in Fig. 4 for the three resonance frequencies f = 1.940 kHz (dash-dotted blue line), 1.951 kHz (dashed black line), and 1.968 kHz (solid red line) at $T = 25$ °C. The borders between the 15 neighboring image frames are marked by vertical dashed black lines (white dashed lines in Fig. 4(a and b)). The channel-center single-image frame is colored light gray. The discontinuity at the fourth border (x = −2.8 mm) is due to a glitch we could not compensate for when switching frame rates.

If we restrict ourselves to observe the image frame in the center of the channel (gray box), we now find that the 1.940-MHz-mode (blue) is the weakest. Moreover, if we in this single frame let the frequency increase from 1.940 MHz to 1.968 MHz, we see how the magnitude of the subsequent resonances increases. This is the spatial structure of the resonances corresponding to the frequency spectra in Fig. 9(b), where the normalized area-average speed increases from 0.05, *via* 0.3 to 0.6 for the three respective frequencies. This observation confirms our conjecture in ref. 20 about the dependence of the locally determined energy density on the spatial structure of the resonance modes.

VI. Application example: focusing efficiency during flow

While the stop-flow mode with time-gated ultrasound actuation at zero flow rate is well suited for characterization of our setup, it is the continuous-flow mode with continuous ultrasound actuation at non-zero flow rate that most often is used in applications. In the following we therefore study the connection between these modes of operation.

The flow focusing efficiency can be characterized by the magnitude of the PZT actuation voltage U_{pp} needed to exactly focus the tracer particles transversely near the outlet of the channel. At this condition the axial transit time equals the transverse focus time, and this special time we denote τ. At the given flow rate of the experiment, $Q = 0.1$ mL min^{-1} = 1.67 × 10^{-9} m^3 s^{-1}, we obtain $\tau = wLh/Q = 1.24$ s from the channel volume and flow rate. If the special focus condition is obtained by the voltage U_{pp}, a theoretical measure of the focus efficiency

can be defined as the voltage-corrected, transverse, average acoustophoretic velocity

$$\langle u_y \rangle = \left(\frac{1\mathrm{V}}{U_{\mathrm{pp}}}\right)^2 \frac{w}{2}\frac{1}{\tau} = \left(\frac{1\mathrm{V}}{U_{\mathrm{pp}}}\right)^2 0.15\,\frac{\mathrm{mm}}{\mathrm{s}}. \qquad (10)$$

In Fig. 11(a) the measured voltage U_{pp} required to focus particles to a predefined region 5 mm before the outlet is plotted *versus* frequency f at the two temperatures $T = 23\,^{\circ}\mathrm{C}$ (red points) and 25 °C (blue points). Based on these data and the definition in eqn (10), we plot in Fig. 11(b) the focus efficiency $\langle u_y \rangle$ *versus* f for the same two temperatures. In agreement with the global stop-flow measurements in Fig. 10, the continuous flow measurements also reveal resonance peaks at the three frequencies $f = 1.940$ MHz, 1.951 MHz, and 1.968 MHz. The values of the focus efficiency at the three resonance frequencies are 105 μm s^{-1}, 32 μm s^{-1}, and 47 μm s^{-1}, respectively. These continuous-flow values are in the same order of magnitude as the respective stop-flow resonance strengths $\Sigma(f) = 51$ μm s^{-1}, 29 μm s^{-1}, and 22 μm s^{-1} obtained in Section V C, but about a factor of 2 larger, as the latter was obtained for one third of the channel length.

Finally, we note that the globally measured shift in resonance frequencies in Fig. 11(b) due to temperature is approximately 2 kHz $^{\circ}\mathrm{C}^{-1}$ which is in agreement with the local velocity measurements of Fig. 9. Notably, the peak at $f = 1.968$ MHz is not significantly shifted in any of the experiments. We have thus established a direct and consistent connection between the stop-flow mode and continuous-flow mode acoustophoretic measurements.

VII. Discussion

We have presented an automated and temperature-controlled experimental platform for characterization of microchannel acoustophoresis by μPIV. The platform was operated in stop-flow mode.

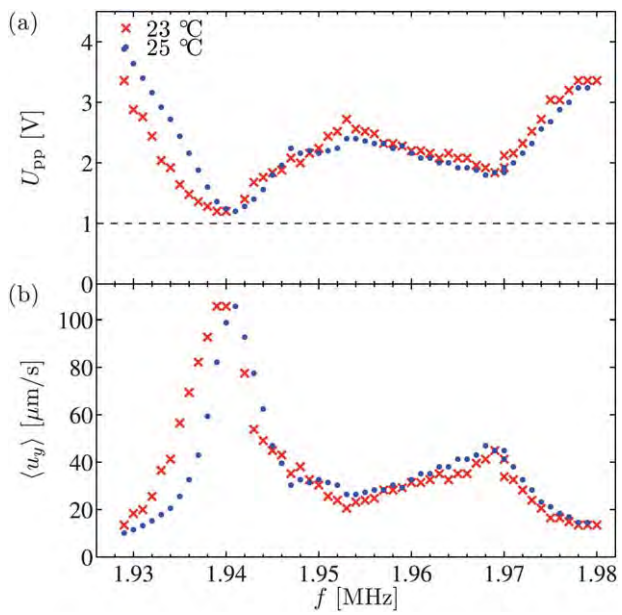

Fig. 11 (a) The measured voltage U_{pp} required to focus particles to a predefined region 5 mm before the outlet of the microchannel ($x = 30$ mm), at an average axial speed $\langle u_x \rangle \approx 0.03$ m s^{-1}. (b) The focus efficiency $\langle u_y \rangle$ obtained by combining eqn (10) with the data for U_{pp} in panel (a).

The high mechanical, thermal, and electronic stability of the platform and the good reproducibility of the measurements provided acoustophoretic velocity data with a spatial resolution of about 20 μm and a relative uncertainty of the velocity measurements of about 5%. The good experimental statistics was enabled by the system automation allowing individual experiments to be repeated 20 to 100 times. The standard deviation of the obtained data can be further reduced, but in practise this is balanced against the time it takes to acquire and analyze the data.

We have demonstrated both short-term stability of the order of 1 h (the time it takes to measure a single frame at a given frequency and temperature), and long-term stability over several days (the time it takes to make multi-frame scans over large sections of the microchannel).

The net total active μPIV experimental time reported in this paper was ~ 60 h corresponding to approximately 7000 gated ultrasound onsets. Furthermore, automated data transfer, image processing, and μPIV-evaluation of the more than 7000 acquired image pairs was carried out in the subsequent data analysis.

We have further shown that temperature control is the key feature to obtain stable and reproducible resonant ultrasound modes in an acoustophoresis microchannel. For minute temperature changes (~2 °C), the acoustic resonance peaks are shifted by ~ 1 kHz/°C. However, a temperature change of 5 °C can lead to a complete change from one resonance mode into another.

In an attempt to capture the global features of some resonant modes it was found that the transverse velocity field varied greatly along the channel. This is indicative of the acoustic resonance having similarities with a box potential. The particle velocity dynamics (> 10-fold) of the system was found to be experimentally very challenging as the quality of the μPIV-analysis benefit from moderate frame-to-frame motion of tracer particles. An iterative scheme was employed, adjusting either camera frame rate or ultrasound intensity to fit the expected velocity magnitude at a certain position.

The large spatial variation in velocity magnitude calls for some concern regarding the strategy that we employed for the frequency spectra data, where a single field of view was evaluated for a range of frequencies. An alternative approach, rather than measuring the resonance peaks in the frequency domain, would be to measure the spatial shifts of the resonant modes. Conversely, spatial shifts of resonances caused by temperature and frequency shifts could give rise to apparent translation of resonance peaks in the frequency domain, which under strict temperature control should be feasible.

The development of our automated μPIV platform has enabled the establishment of a direct and consistent connection between the stop-flow mode and continuous-flow mode acoustophoretic measurements. As the latter essentially is a area-average of the acoustophoretic velocity, the most direct comparisons were conducted on the global stop-flow measurements.

With this work we have advanced acoustophoretic characterization methods considerably since our automated μPIV method leads to more accurate and rapid determination of the local

acoustic energy density. We have in the present work been able to confirm the conjecture in our former work on how the locally determined energy density depends on the spatial structure of the resonance modes.

The complexity of the acoustic resonance patterns in this type of resonator requires further studies of the frequency, temperature, and spatial domain. This vast parameter space calls not only for automation, but also, predictive models are needed to better understand acoustophoresis. In this work we have pinpointed some of the minimum requirements on an experimental approach for detailed measurements and analysis of microchannel acoustophoresis.

VIII. Conclusions

Long-term, reproducible, and quantitative assessment of acoustic standing wave forces in microchannels has to a very limited degree been reported in the literature. This paper outlines an effort to standardize the characterization of microchannels intended for acoustophoresis, and an optimized μPIV setup and its use as a powerful analytical tool to high resolution characterization of the acoustophoretic properties of microchannels is reported.

The obtained high accuracy μPIV data allows for in-depth analysis of the influence of systemic parameters on the acoustophoresis performance such as temperature and we propose a normalized measure to describe acoustophoresis channels in terms of its ability to focus particles in continuous flow. The importance of analyzing system response to the actuation frequency in relation to the employed PZT voltage is highlighted, and most importantly we demonstrate the strong dependence of the obtained microchannel resonances with respect to temperature, which calls for a strict temperature control in all acoustophoresis systems of analytical grade.

Based on these developments we now anticipate the use of this system as a standard tool to normalize the performance of different microchannels as well as to decouple other forces acting on particles/cells in the primary acoustic standing wave field. Most importantly, the μPIV system will enable the measurement of fundamental acoustophysical properties such as acoustophoretic mobility of different particle and cell species in various buffer systems. We will continue to build on the interplay between experiment and theoretical predictions such that we can broaden the understanding of the critical system parameters in acoustofluidics and hence facilitate an engineering-based computational approach to acoustophoresis system design.

Acknowledgements

This research was supported by the Danish Council for Independent Research, Technology and Production Sciences, Grant No. 274-09-0342; the Swedish Research Council, Grant No. 2007-4946; and the Swedish Governmental Agency for Innovation Sybstems, VINNOVA, the programme Innovations for Future Health, Cell CARE, Grant No. 2009-00236.

References

1 J. Hawkes, D. Barrow, J. Cefai and W. Coakley, *Ultrasonics*, 1998, **36**, 901–903.
2 J. J. Hawkes and W. T. Coakley, *Sens. Actuators, B*, 2001, **75**, 213–222.
3 N. R. Harris, M. Hill, S. Beeby, Y. Shen, N. M. White, J. J. Hawkes and W. T. Coakley, *Sens. Actuators, B*, 2003, **95**, 425–434.
4 A. Nilsson, F. Petersson, H. Jönsson and T. Laurell, *Lab Chip*, 2004, **4**, 131–5.
5 F. Petersson, A. Nilsson, C. Holm, H. Jönsson and T. Laurell, *Analyst*, 2004, **129**, 938–43.
6 P. Augustsson, J. Persson, S. Ekström, M. Ohlin and T. Laurell, *Lab Chip*, 2009, **9**, 810–818.
7 C. Grenvall, P. Augustsson, J. R. Folkenberg and T. Laurell, *Anal. Chem.*, 2009, **81**, 6195–6200.
8 P. Thevoz, J. D. Adams, H. Shea, H. Bruus and H. T. Soh, *Anal. Chem.*, 2010, **82**, 3094–3098.
9 J. Shi, D. Ahmed, X. Mao, S.-C. S. Lin, A. Lawit and T. J. Huang, *Lab Chip*, 2009, **9**, 2890–2895.
10 T. Franke, S. Braunmueller, L. Schmid, A. Wixforth and D. A. Weitz, *Lab Chip*, 2010, **10**, 789–794.
11 G. T. Haar and S. Wyard, *Ultrasound Med. Biol.*, 1978, **4**, 111–123.
12 R. J. Townsend, M. Hill, N. R. Harris and N. M. White, *Ultrasonics*, 2004, **42**, 319–324.
13 S. M. Hagsäter, T. G. Jensen, H. Bruus and J. P. Kutter, *Lab Chip*, 2007, **7**, 1336–1344.
14 S. M. Hagsäter, A. Lenshof, P. Skafte-Pedersen, J. P. Kutter, T. Laurell and H. Bruus, *Lab Chip*, 2008, **8**, 1178–1184.
15 J. Shi, H. Huang, Z. Stratton, Y. Huang and T. J. Huang, *Lab Chip*, 2009, **9**, 3354–3359.
16 O. Manneberg, J. Svennebring, H. M. Hertz and M. Wiklund, *J. Micromech. Microeng.*, 2008, **18**, 095025.
17 O. Manneberg, B. Vanherberghen, B. Onfelt and M. Wiklund, *Lab Chip*, 2009, **9**, 833–837.
18 J. D. Adams, P. Thevoz, H. Bruus and H. T. Soh, *Appl. Phys. Lett.*, 2009, **95**, 254103–1.
19 P. Augustsson, R. Barnkob, C. Grenvall, T. Deierborg, P. Brundin, H. Bruus and T. Laurell, *Proc. 14th MicroTAS*, 3–7 October 2010, Groningen, The Netherlands, 2010, pp. 1337–39.
20 R. Barnkob, P. Augustsson, T. Laurell and H. Bruus, *Lab Chip*, 2010, **10**, 563–570.
21 L. P. Gorkov, *Soviet Physics - Doklady*, 1962, **6**, 773–775.
22 J. Lighthill, *Waves in Fluids*, Cambridge University Press, 2002.
23 A. D. Pierce, *Acoustics*, Acoustical Society of America, Woodbury, 1991.
24 H. Bruus, *Theoretical Microfluidics*, Oxford University Press, Oxford, 2008.
25 J. Santiago, S. Wereley, C. Meinhart, D. Beebe and R. Adrian, *Exp. Fluids*, 1998, **25**, 316–319.
26 R. Adrian, *Exp. Fluids*, 2005, **39**, 159–169.
27 M. Raffel, C. E. Willert, S. T. Wereley and J. Kompenhans, *Particle Image Velocimetry*, Springer, 2007.
28 R. Lindken, M. Rossi, S. Grosse and J. Westerweel, *Lab Chip*, 2009, **9**, 2551–2567.
29 S. T. Wereley and C. D. Meinhart, *Annu. Rev. Fluid Mech.*, 2010, **42**, 557–576.
30 C. Meinhart, S. Wereley and J. Santiago, *J. Fluids Eng.*, 2000, **122**, 285–289.
31 R. Adrian, *Appl. Opt.*, 1986, **25**, 3855–3858.

